



Effect of intrinsic point defects on the catalytic and electronic properties of Cu_2WS_4 single layer: *Ab initio* calculations

Tarik Ouahrani * and Reda M. Boufatah

Laboratoire de Physique Théorique, Université de Tlemcen, Tlemcen 13000, Algeria

Mohammed Benaissa

Laboratory of Materials Discovery, Unit of Research Materials and Renewable Energies, LEPM-URMER, Université de Tlemcen, Tlemcen 13000, Algeria

Ángel Morales-García 

Departament de Ciència de Materials i Química Física and Institut de Química Teòrica i Computacional, Universitat de Barcelona, c/Martí i Franquès 1-11, 08028 Barcelona, Spain

Michael Badawi 

Université de Lorraine, LPCT, UMR 7019, 54506 Vandoeuvre-lès-Nancy, France

Daniel Errandonea †

Instituto de Ciencia de Materiales, Matter at High Pressure (MALTA) Consolider Team, Departamento de Física Aplicada, Universidad de Valencia, Edificio de Investigación, C/Dr. Moliner 50, Burjassot, 46100 Valencia, Spain



(Received 22 September 2022; revised 30 December 2022; accepted 8 February 2023; published 17 February 2023)

The challenges imposed by climate change require the continued improvement and identification of materials for the development of green technologies. Point defect engineering is a promising technology for producing green hydrogen by taking advantage of catalytic hydrogen evolution reactions. In this work, we investigate the role of anionic and cationic vacancy point defects, as well as the nature of the active sites, in the catalytic activation of Cu_2WS_4 single layers. The stability of the pristine and defective structures of Cu_2WS_4 has been thoroughly investigated using density-functional theory calculations. A deep analysis of the formation enthalpy indicates that the Cu vacancy is the chemically most favorable vacancy. However, the calculated adsorption energy indicates that the presence of such vacancies slightly enhances the hydrogen evolution reaction. In contrast, the formation of an S vacancy considerably magnifies the same reaction in Cu_2WS_4 single layers.

DOI: [10.1103/PhysRevMaterials.7.025403](https://doi.org/10.1103/PhysRevMaterials.7.025403)

I. INTRODUCTION

Today, the need to develop green sources of energy is becoming urgent due to climate change and environmental concerns. The core of clean-energy production is based on the use of water to produce green hydrogen. The progress on this technology requires the creation of catalytic materials with high efficiency for the production of hydrogen through the process of water electrolysis. The hydrogen evolution reaction (HER) is one of the most promising mechanisms [1,2]. Nowadays, HER-based technologies are dominated by the use of platinum-based catalysts. However, the high cost, low supply, and scarcity of this noble metal severely limit its practical applications for large-scale hydrogen production [3–5]. In addition, Pt is a heavy element, and thus, its use in electrodes for electrocatalysis could have harmful effects

on human health [6]. These facts make the search for cheap and abundant alternatives to Pt-based materials extremely important. To be a good candidate for HER applications, the material should be a good electrocatalyst to adsorb hydrogen. Nowadays, the search for alternatives to Pt-based materials is focused on the use of two-dimensional (2D) materials, namely, 2D transition metal dichalcogenides (TMDs) [7–10]. However, the bare structure of most TMDs shows weakness in binding H atoms at their surfaces, and defective sites are then used to overcome this problem [11]. Recent studies showed that the presence of defect sites on a structure locally alters the electronic properties. Such a site on the surface of TMDs can trap hydrogen atoms, forming new synergetic bonds with them [12–14]. To enable progress in the use of TMDs in HER-based technologies, a rigorous assessment of catalytic and electronic properties is needed.

Defects influence the performance of most functional materials and devices. They can strongly affect the electrocatalytic properties. Defects can take many forms. They can be vacancy defects, interstitial defects, nonmetallic atom doping, and metal-defect coordination structures. Even a low

*Also at École supérieure en sciences appliquées, Boîte Postale. 165, Tlemcen 13000, Algeria; tarik.ouahrani@univ-tlemcen.dz

†daniel.errandonea@uv.es

concentration of defects, which is difficult to detect in experiments, can affect the electronic properties of materials. Recently, several methods were elaborated to manufacture defect-based motifs in low-dimensional structures [15]. Potentially, these methods can be employed to improve the HER functionality of materials [16–20]. An open question regarding the influence of defects on HER activity is how the activation of catalytic sites is related to the nature of defects. In an attempt to respond to this question, in this study we analyze the effect of the intrinsic defects on the Cu_2WS_4 layered structure. Cu_2WS_4 can be easily and cheaply synthesized by means of solvothermal methods [21]. It has also been built as CuWO_4/CuO heterojunctions using wet-based techniques or as a combination of $\text{CuWO}_4/\text{WO}_{3-x}$ layers prepared by reactive sputtering for thin-film applications [22–24]. Experiments showed that Se-doped Cu_2WS_4 has an interesting HER activity with a very low onset potential of -0.32 V at 10 mA/cm² current density with a 46 mV/dec Tafel slope [25]. Tiwari *et al.* [25] attributed the increased electrocatalytic activity in doped Cu_2WS_4 to an abundance of active sites caused by the substitution of S by Se atoms. For the same reason, a defective structure should also be tested to analyze the HER reactivity. Motivated by this challenge, we investigated by means of the density-functional theory (DFT) method the effect of intrinsic defects on electrocatalytic reactivity in Cu_2WS_4 . In particular, we focused on cation vacancy defects. To simulate such a system, we employed the Freysoldt method. [26,27]. It allowed us to unveil more favorable defect structures by identifying the ground state and, at the same time, examining the impact of each defect on the adsorption of H_2 on 2D Cu_2WS_4 [28]. In particular, we will discuss how the HER activity is affected by the nature of the defect and that of the adsorbed site.

II. COMPUTATIONAL DETAILS

DFT calculations were carried out with the Vienna Ab initio Simulation Package (VASP) [29–31] using the projector augmented wave method [32] and a plane-wave cutoff of 550 eV. Geometry optimizations were done using the Perdew-Burke-Ernzerhof (PBE) exchange and correlation functionals [33] within a spin-polarized framework. Total energies were considered to have converged with an accuracy of 10^{-6} eV. Gaussian smearing with a width of 0.05 eV was used for the Brillouin zone integration using a k -point grid within the Monkhorst-Pack scheme [34] with a $7 \times 7 \times 1$ k mesh ($3 \times 3 \times 1$ for supercell calculations). A Grimme with Becke-Jonson damping [35,36] dispersion correction (DFT-D3/BJ) was included to describe the contribution of London dispersion interactions. A vacuum of 20 Å was used along the \mathbf{z} axis to avoid interactions between the adjacent molecules and slabs. *Ab initio* molecular-dynamics (AIMD) simulations were performed using the Nosé-Hoover thermostat approach [37–39] at a temperature of 300 K with a time step of 0.5 fs. Phonon dispersions were calculated using PHONOPY [40], which was interfaced with the VASP code. We used the force constant supercell method [41].

To analyze the electrocatalytic HER activity we used the formalism developed by Nørskov *et al.* [42]. In this approach, the relative hydrogen adsorption free energies ΔG_H are calculated in the acid solution using the standard hydrogen

electrode model as follows [43]:

$$\Delta G_H = \Delta E^{\text{tot}} - T \Delta S + \Delta E^{\text{ZPE}} \quad (1)$$

The terms ΔE^{tot} , $T \Delta S$, and ΔE^{ZPE} denote the differences in DFT total energies, entropic contributions, and zero-point energies, respectively. They can be derived from computations of the vibrational frequencies and standard thermodynamic data. ΔE^{tot} gives the adsorption energy for adding one H atom to the studied structure. It can be calculated as $E_{\text{ads}} = E_{\text{def-Cu}_2\text{WS}_4+\text{H}} - E_{\text{def-Cu}_2\text{WS}_4} - 1/2E(\text{H}_2)$. $E_{\text{def-Cu}_2\text{WS}_4+\text{H}}$ represents the total energy of the optimized H adsorption configuration. $E_{\text{def-Cu}_2\text{WS}_4}$ and $E(\text{H}_2)$ stand for the energies of the calculated defect structure and target hydrogen molecule, respectively.

In addition, to reveal the energetically most preferable defect structure, the formation energy of the defect D_q in a charged state $q(E_f(D^q))$ was obtained with the following formula [26]:

$$E_f(D^q) = E_{\text{tot}}(C : D^q) - E_{\text{tot}}(C) - \sum_i \Delta n_i \mu_i + q(\epsilon_{\text{VBM}} + \epsilon_F) + E_{\text{corr}}, \quad (2)$$

where $E_{\text{tot}}(C : D^q)$ is the total energy of the supercell containing the defect and $E_{\text{tot}}(C)$ is the total energy of the perfect crystal supercell. E_{corr} corresponds to the correction energy used to overcome the periodic interaction between charges in doped systems. The charge state q was taken here to be -2 , -1 , 0 , $+1$, and $+2$. Finally, the term μ_i is the atomic chemical potential of an atom reservoir of an element i ; it can be added ($\Delta n_i = +1$) or removed ($\Delta n_i = -1$) from the supercell. Finally, ϵ_{VBM} and ϵ_F denote, respectively, the eigenvalue of the valence-band maximum (VBM) state and the Fermi level E_F . For complementary information about this scheme, readers are referred to Ref. [44]. In order to simulate accurately the transition levels and the band gap, the Heyd-Scuseria-Ernzerhof (HSE) hybrid density functional (HSE06) [45] was used to relax the point defect structures.

III. RESULTS AND DISCUSSION

A. Stability of the pristine Cu_2WS_4 single layer

We will first evaluate the stability of the studied structures. For this purpose, a full optimization was carried out on the pristine structure. The calculated PBE + D3/BJ lattice parameter (5.43 Å) agrees with experiments [28] and previous calculations [46]. The formation energy, phonon dispersion, and elastic constants were also calculated for the optimized Cu_2WS_4 single layer. In Fig. 1 we show the phonon dispersion. The absence of imaginary branches indicates that 2D Cu_2WS_4 is dynamically stable. Our calculated phonon dispersion is similar to that previously reported for Cu_2WS_4 [13] and Cu_2MoS_4 [47]. The phonon dispersion has 21 branches. Three are acoustic, and the rest are optical modes. A point group symmetry analysis of the modes at the center of the Brillouin zone gives $\Gamma = 2A_1 + 2A_2 + B_1 + 4B_2 + 6E$, where $\Gamma_{\text{acoustic}} = B_2 + E$ and $\Gamma_{\text{optic}} = 2A_1 + 2A_2 + B_1 + 3B_2 + 5E$. The $2A_1 + B_1 + 3B_2 + 5E$ modes are Raman active. The $3B_2 + 5E$ modes are also infrared active. The A_2 modes are silent. The calculated wave numbers are summarized in

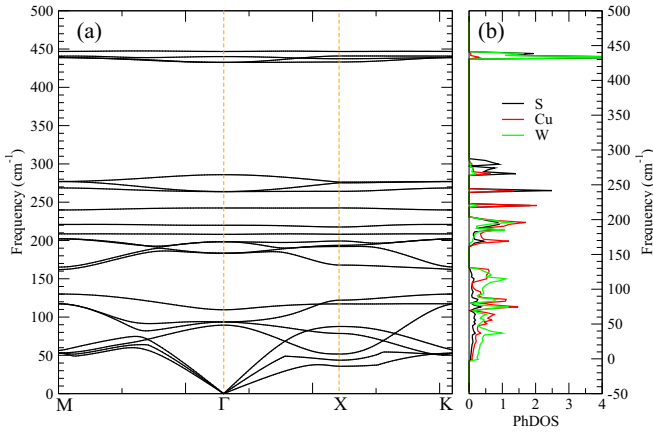


FIG. 1. (a) Phonon dispersion and (b) phonon density of states of the Cu_2WS_4 single layer.

Table I. Unfortunately, no experimental data are available to make a comparison, and previous calculations do not report calculated wave numbers [13].

The mechanical properties of 2D Cu_2WS_4 were also calculated through the elastic stiffness components using the stress-strain relation implemented in VASPKIT [48]. The C_{11} and C_{12} components are given in Table S1 of the Supplemental Material (SM) [49]. They fulfill the Born-Huang ($C_{11} > 0$ and $C_{11} - C_{12} > 0$) conditions [50,51], an indication of the mechanical stability of the Cu_2WS_4 monolayer. Mechanical properties were also analyzed through the Young's modulus E and shear modulus G , which are given in Table S1 of the SM [49]. Based on the values of E and G , we can state that 2D Cu_2WS_4 is a ductile material. In particular, the application of forces on the transverse section during uniaxial tension or compression will weakly affect the structure.

B. Stability of native point defects in the Cu_2WS_4 monolayer

1. Chemical stability of point-defect-free Cu_2WS_4

In this work, we consider native defects, which are point defects inherent in Cu_2WS_4 . Three potential point defect

TABLE I. Calculated modes of 2D Cu_2WS_4 . Raman (R), infrared (IR), and silent (S) modes are indicated.

Symmetry	ω (cm^{-1})	Activity
A_2	87.3	S
E	87.9	R-IR
B_2	109.0	R-IR
E	177.6	R-IR
E	195.8	R-IR
B_2	207.2	R-IR
A_1	215.1	R
A_2	237.8	S
E	259.6	R-IR
B_1	280.8	R
E	428.4	R-IR
B_2	436.3	R-IR
A_1	441.4	R

structures are considered. To simulate the effect of missing atoms, we built structures with sulfur [V(S)], copper [V(Cu)], and tungsten [V(W)] vacancies [52] (see Fig. 2). To reduce the artificial self-image interactions imposed by periodic-boundary conditions [53], some convergence tests were done on a number of enlarged supercells, namely, $2 \times 2 \times 1$, $3 \times 2 \times 1$, $3 \times 3 \times 1$, $4 \times 4 \times 1$, $5 \times 5 \times 1$, and $6 \times 6 \times 1$. Here, we compute the uniform supercell scaling behavior within dielectric continuum theory using the SXDEFECTALIGN2D tool, applying standard 2D charge corrections [54–56]. The energy formation of these structures was calculated and is displayed in Figs. S1(a) and S1(b) in the SM [49]. For example, the plots related to the sulfur/copper defect point structure indicate that the size of a $4 \times 4 \times 1$ supercell of 112 atoms is enough to prevent artificial self-interaction between the defect and its image (see Table S2 in the SM [49]). Thus, the concentration of the defect in this structure is able to simulate a realistic concentration of 0.893% of vacant atoms. The size of the studied structures is a compromise between accuracy and computing demands. To assess the energetic stability of the defective structures, their formation energies were estimated using the Freysoldt formulation [26]. The defect formation energy as a function of chemical potential gives information about the reliability of building the studied defective structures.

In order to investigate the effect of the intrinsic defects on the HER reaction, we first estimate the thermodynamic stability of the studied pristine structure. The chemical potentials of the constituent atoms of the Cu_2WS_4 monolayer obey a number of restrictions based on the energetic equilibrium. Such conditions maintain a stable Cu_2WS_4 compound. They include

$$2\Delta\mu_{\text{Cu}} + \Delta\mu_{\text{W}} + 4\Delta\mu_{\text{S}} = \Delta E(\text{Cu}_2\text{WS}_4), \quad (3)$$

where μ_{Cu} , μ_{W} , and μ_{S} are the chemical potentials of Cu, W, and S. $\Delta E(\text{Cu}_2\text{WS}_4)$ is the corresponding formation enthalpy. Because $\mu_i = 0$ indicates the element i will be formed as a pure element, $\mu_{\text{Cu}} < 0$, $\mu_{\text{W}} < 0$, and $\mu_{\text{S}} < 0$ should be satisfied to ensure that no elemental phases of Cu, W, or S coexist with Cu_2WS_4 . The conditions that must be met as constraints to guarantee the formation of the compound, including all relevant competing phases, are given in Table S2 in the SM [49]. Based on them, we determined the chemical potential region that stabilizes a pure Cu_2WS_4 monolayer. Results are plotted in Figs. 3–5. The chemical potentials μ_{Cu} , μ_{W} , and μ_{S} were used as the dependent variables in three different cases. The small stability area means that the growth of stoichiometric Cu_2WS_4 is not easy because many competitive secondary phases could form. The resulting intersection points bounding the stability regions show that when μ_{Cu} and μ_{S} are dependent variables, the growth promotes the appearance of a Cu vacancy along points A (S rich, W poor, Cu rich) and E (S poor, W rich, Cu rich). Cu_2WS_4 competes only with Cu_2S_2 at point A. There are more chances of having a Cu vacancy in Cu_2WS_4 at point A (see Fig. 4). At the same time, this condition promotes the appearance of a W vacancy along points A (S rich, W rich, Cu rich) and B (S rich, W rich, Cu rich; see Fig. 5). Cu_2WS_4 competes only with WS_2 at point B. We are more likely to have a W vacancy in Cu_2WS_4 at point B. However, obviously, according to Fig. 3, the line of the Cu_2WS_4 component is not the limit of the formation domain;

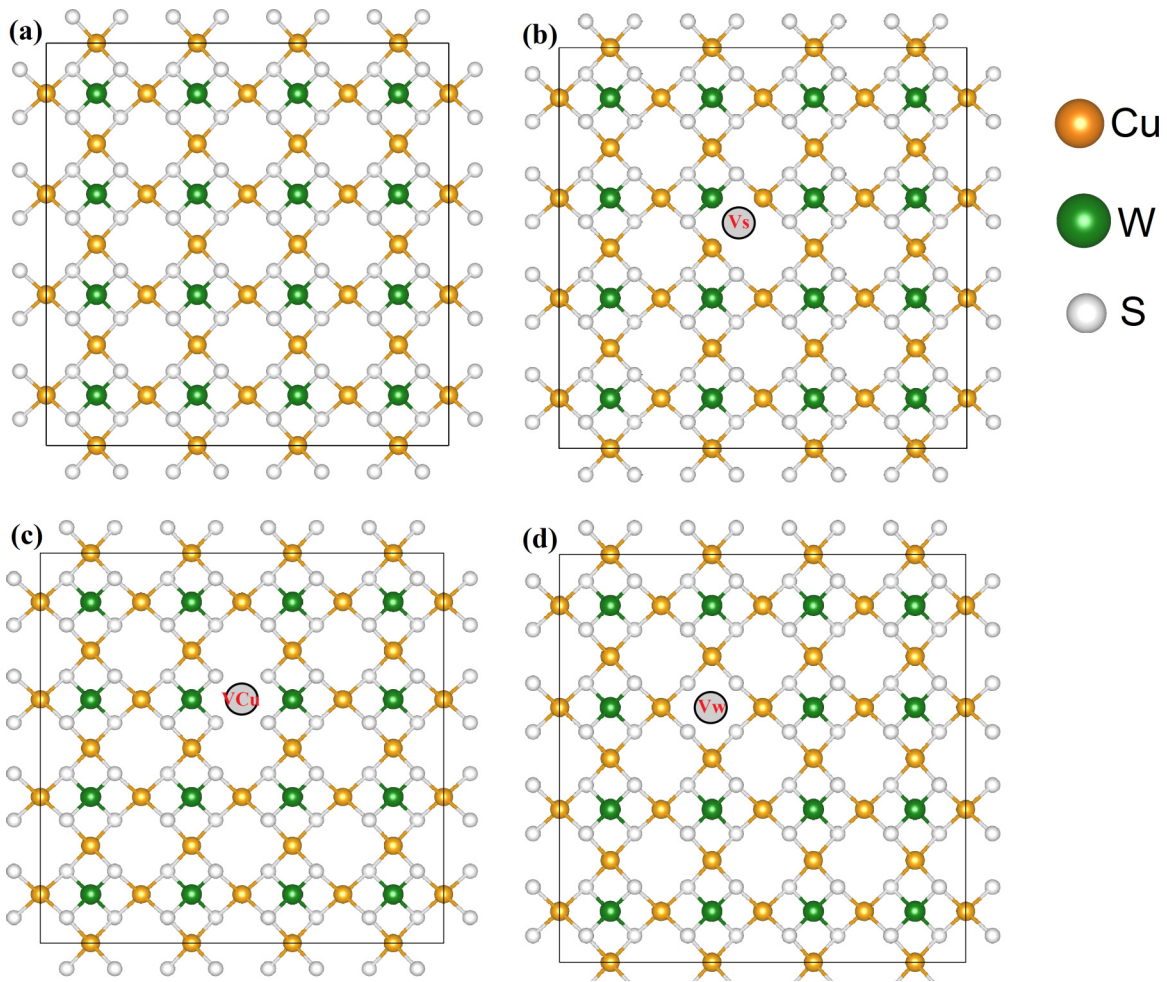


FIG. 2. Optimized structures of point defects: (a) the pristine structure, (b) sulfur vacancy [V(S)], (c) copper vacancy [V(Cu)], (d) and tungsten vacancy [V(W)] in a $4 \times 4 \times 1$ cell.

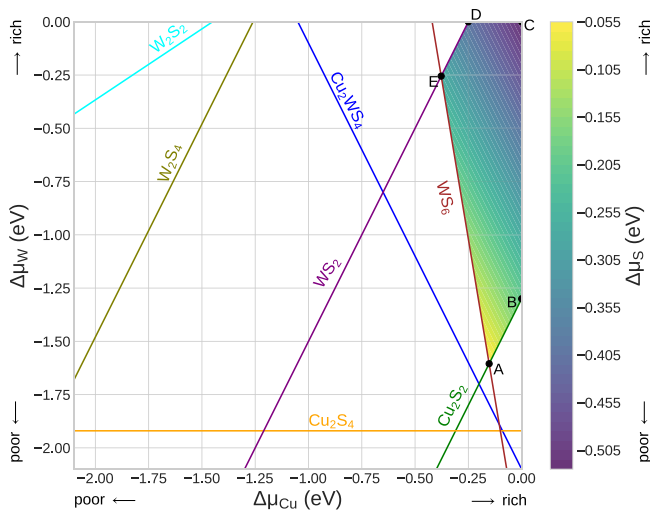


FIG. 3. Chemical potential phase diagram showing the region of stability of defective Cu_2WS_4 . We show the variation in $\Delta\mu_S$ as a function of $\Delta\mu_W$ and $\Delta\mu_{\text{Cu}}$ within the stability region. Colored lines are the limits imposed by competing phases. A, B, C, D, and E delimit the stability area and represent the intersections points of conditions given in Table S3 in the SM [49].

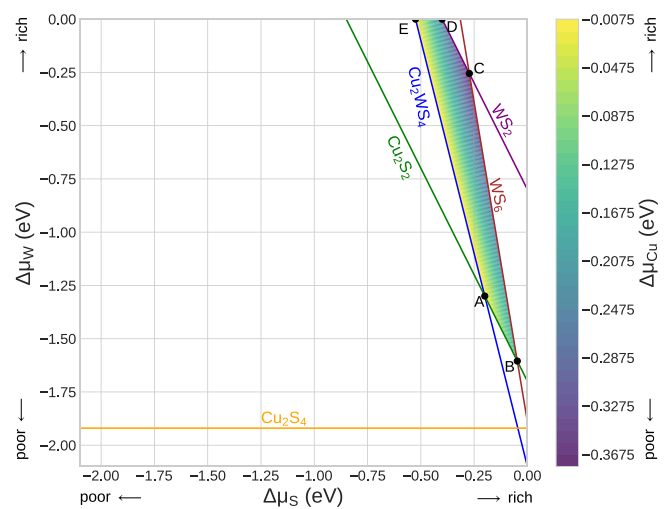


FIG. 4. Chemical potential phase diagram showing the region of stability of defective Cu_2WS_4 . We show the variation in $\Delta\mu_{\text{Cu}}$ as a function of $\Delta\mu_S$ and $\Delta\mu_W$ within the stability region. Colored lines are the limits imposed by competing phases. A, B, C, D, and E delimit the stability area and represent the intersections points of conditions given in Table S3 in the SM [49].

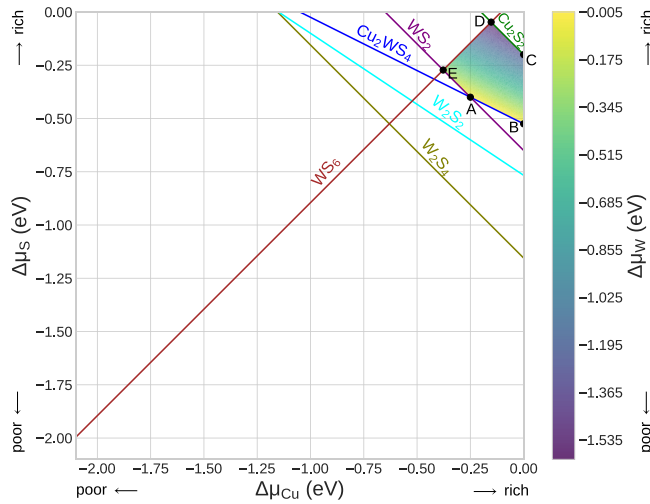


FIG. 5. Chemical potential phase diagram showing the region of stability of defective Cu_2WS_4 . We show the variation in $\Delta\mu_W$ as a function of $\Delta\mu_S$ and $\Delta\mu_{\text{Cu}}$ within the stability region. Colored lines are the limits imposed by competing phases. A, B, C, D, and E delimit the stability area and represent the intersections points of conditions given in Table S3 in the SM [49].

this implies that the Cu_2WS_4 structure is less advantageous for growing a system with a S vacancy.

2. Chemical stability of Cu_2WS_4 with point defects

To calculate the formation energies of different point defects as a function of chemical potential, we use Eq. (2), but without incorporating the $q(\epsilon_{\text{VBM}} + \epsilon_F) + E_{\text{corr}}$ term. We can show that the formation energy corresponding to $\text{V}(\text{Cu})$ gives a lower value, which reinforces the conclusion stated

before using Eq. (3). The results are displayed in Fig. S2 in the SM [49]. This plot shows the variation of $E_f(D^0)$ with regard to the Cu rich/poor environments and W rich/poor environments. We can observe that the defects of $\text{V}(\text{Cu})$ have a lower defect formation energy under both poor Cu and W growth conditions. The negative formation energy indicates that the defective $\text{V}(\text{Cu})$ and $\text{V}(\text{W})$ structures are more stable than the $\text{V}(\text{S})$ ones.

In contrast, due to their high formation energies, $\text{V}(\text{W})$ and $\text{V}(\text{S})$ are thermodynamically less favorable. The transition level was calculated at the HSE06 level, and it is displayed in Fig. 6. The difference between VBM and conduction-band minimum (CBM) levels agrees well with the band gap of pristine Cu_2WS_4 calculated using the hybrid HSE06 functional (~ 2.5 eV). Lines with the most stable q are shown for each chemical potential. Figure 6 depicts a charge value of q for each line. It is shown that $2+$, $2-$, and $1+$ charge states do not belong to the transition levels. The formation energies of the charged defects vary with the Fermi level, in which the slopes correspond to their charge states as defined by Eq. (2). We can see that $\text{V}(\text{W})$ and $\text{V}(\text{S})$ are relatively unstable compared to $\text{V}(\text{Cu})$, which confirms that Cu point defects are more favorable in the Cu_2WS_4 monolayer. Furthermore, when we look at the transitions near the CBM, we see that $\text{V}(\text{Cu})$ for $q = 0$ is in the vicinity of the CBM, evidencing an electronically neutral defect. According to the HSE06 calculated transitions states, the Cu vacancy has a low formation energy defect with a deep $1-/0$ acceptor level.

Further analyses were done to check the thermal stability of defect vacancy structures. To this end, we used an AIMD simulation within the NVT ensemble controlled by the Nose-Hoover method [37–39]. In Fig. 7, we can see that both total energy and temperature oscillations at ambient conditions

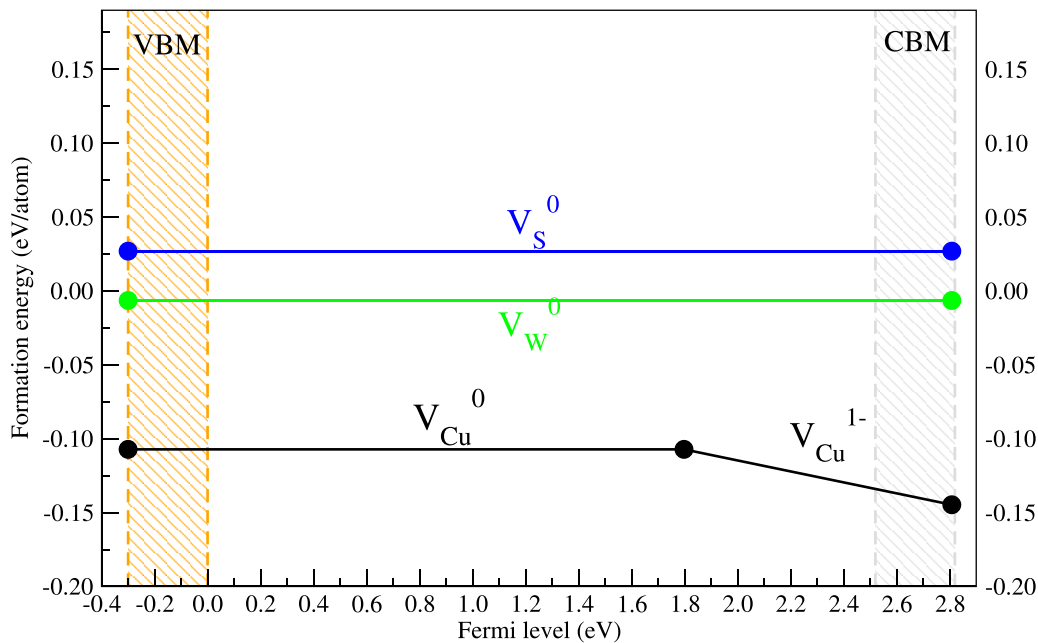


FIG. 6. Schematic illustration of formation energy $E_f(D^q)$ vs Fermi level E_F in three charge states q : 0 and $1-$. Solid lines correspond to the formation energy as defined by Eq. (2). The transition levels correspond to the HSE06 calculations. CBM (VBM) denotes the conduction-band minimum (valence-band maximum). The difference between CBM and VBM levels gives the band gap value.

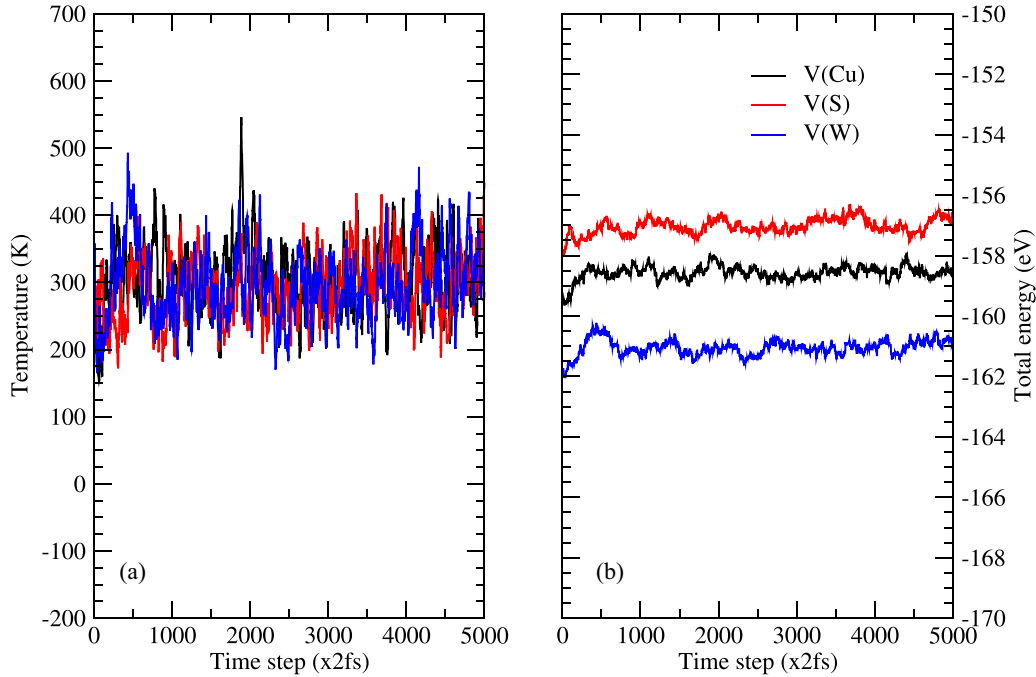


FIG. 7. AIMD simulation of (a) temperature oscillations and (b) energy fluctuations as a function of time step at $T = 300$. Black, red, and blue show V(Cu), V(S), and V(W) defect structures.

show a periodic oscillation. This behavior is proof there is no bond-breaking or structural distortion in the AIMD simulation. In summary, the defect structures of V(Cu), V(S), and V(W) retain their thermal stability under 300 K.

C. Hydrogen evolution reaction analysis

Next, we focus on the electrocatalytic performance of the HER activity. We started analyzing the most stable adsorption sites for atomic H species. Different active sites to anchor H on the surface of three defect structures have been considered (see Fig. S3 in the SM [49]): (i) top sites over W, Cu, and S atoms, (ii) bridge sites in the Cu-S and W-S bonding directions, and (iii) top sites over the vacancy sites. In most cases, the energy adsorption is systematically lower on the top S sites and bridge S-W sites, showing $E_{\text{ads}} = -0.24$ and -0.21 eV, respectively. The same finding was reported in Ref. [46] with regard to Hg atoms. Next, to characterize the catalytic activity of the three structures, the Gibbs free energy of hydrogen adsorption was calculated on the most active sites and is depicted in Fig. 8. We note here that a small ΔG_H value induces strong interaction of adsorbed H, while a large ΔG_H is interpreted as a poor interaction of adsorbed H that is negative for catalytic purposes because it slows down HER kinetics. Among the active sites analyzed, the adsorption on the top Cu and top S atoms in the V(W) defect structure shows a negative Gibbs free energy. This suggests that the interaction of these structures with H atoms is too strong to release H_2 from the catalytic sites. The adsorption of the H nearest neighbor of top Cu sites in the V(Cu) structure exhibits the same behavior. The adsorption on the bridge S-W site for V(Cu) and V(S) structures and on the top S for V(S) and V(W) defect structures provides four cases of interest for HER reactions. The corresponding ΔG_H values are -0.23 , -0.17 ,

0.16 , and -0.18 eV, respectively (see also Table S3 in the SM [49]). They are relatively close to zero, indicating the high HER activity in these cases. Furthermore, the calculated ΔG_H value for the V(S) structure agrees well with that investigated using a different method in previous studies [14], which found ΔG_H equal to -0.14 eV. It is noted that a small difference in the ΔG_H value is probably due to the larger structure used in this study, defined as 1/112 coverage.

As a complementary study, we investigated the electronic properties. The defect-free structure's band structure and partial density of states (PDOS) were calculated (see Figs. S4 and

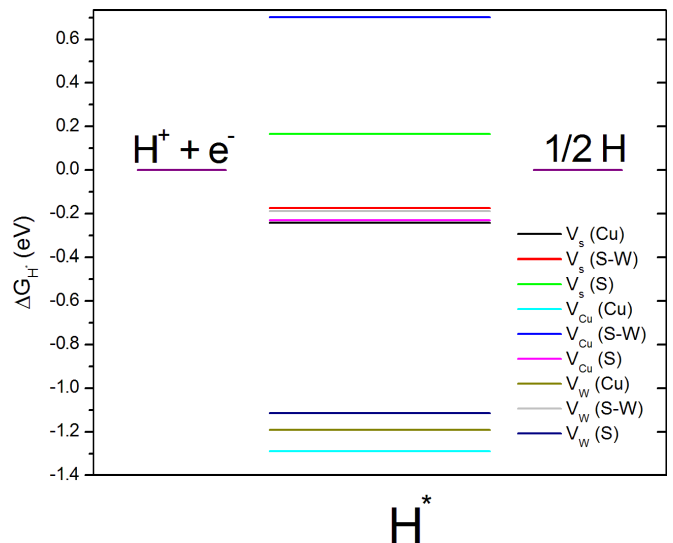


FIG. 8. Schematic Gibbs free energy diagram of HER processing on defective V(S), V(Cu), and V(W) structures located at the top of the Cu atom, on the bridge (S-W), and on the top of the S atom.

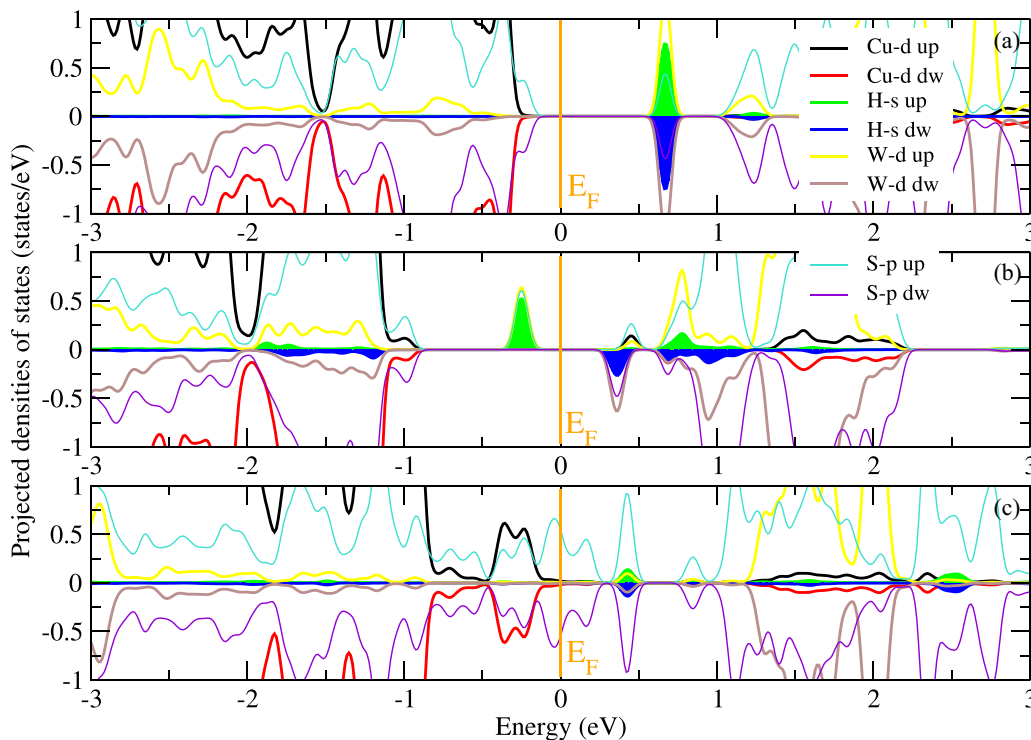


FIG. 9. Partial densities of states of (a) V(Cu)@H⁺, (b) V(S)@H⁺, and (c) V(W)@H⁺ defective structures.

S5 in the SM [49]). The band gap has an indirect nature, and its values within the HSE06 and PBE generalized gradient approximation approaches were found to be, respectively, 2.49 and 1.60 eV. The differences are related to the well-known fact that PBE tends to underestimate band gap energy. [57] The structure also has conductivity values of 5980 and 22 887 ($\Omega \text{ m}$)⁻¹ in the *xx* and *yy* directions, respectively. The removal of the S atom from the pristine structure does not close the band gap energy (see the PDOS in Fig. S6 in the SM [49]). We can see that the spin-down channel is weakly altered by the removal of the sulfur atom. However, Figs. S7 and S8 in the SM [49] show that the removal of Cu/W cations affects the investigated structures. In the case of the copper defect point structure, Cu *d*, Cu *p*, and S *p* acceptor levels are introduced near the top of the valence band, occupying the Fermi level, which obviously moves to the upper energy regions. We can show the formation of acceptor levels of both Cu *d* and S *p* near the Fermi level. In the case of the tungsten defect point structure, the closing of the band gap is more pronounced, with an occupation of both W *d* and W *p* orbitals of the Fermi level (see Fig. S9 in the SM [49]). Both the Cu *d* and *s* and S *p* orbitals have a significant impact on the spin-down channel.

Additional calculations were done for the adsorbed defective structures. Figure 9 shows the spin-polarized PDOS plots of V(S), V(Cu), and V(W) structures with adsorbed H atoms. While both V(Cu)@H⁺ and V(S)@H⁺ show a semiconducting nature, V(W)@H⁺ remains metallic. It is interesting to note that the states of the H* adsorbed atom behave differently in the three cases. In the case of V(S)@H⁺, the electron from the H 1*s* orbital fills one spin-up channel of one defect band, resulting in a strong hybridization with both W *d* and S *p* states. We observe a weak magnetization occurring due to electron transfer between both spin-up and spin-down chan-

nels. The hybridization state spin up shifts below the Fermi level, and in the case of spin down, it lies above this level. However, we do not see a change in V(Cu)@H⁺, but there is a strong hybridization between S *p*/W *d* and H *s* states in both spin-up and spin-down channels. We must highlight that the same trend was observed in the work of Wu *et al.* [14]. Finally, the emergence of partially filled S *p* states at the Fermi level in the case of V(W)@H⁺ renders the adsorption site metallic in nature.

A qualitative survey can be used in order to analyze the correlation of the HER activity with the interaction strength between the intermediate hydrogen atoms and the studied surfaces. This can be achieved by plotting a volcanolike plot of hydrogen binding energy (HBE; see Fig. 10 and Table S3 in the SM [49]). Here, the exchange current density i_0 reflects the intrinsic rate of proton transfer from the H atom to the defect point structure of the Cu₂WS₄ monolayer. In the volcano curve, i_0 is calculated as a function of ΔG_H of hydrogen adsorption according to Nørskov's assumption: If $\Delta G_H < 0$, the proton transfer is exothermic and is calculated at pH = 0 as

$$i_0 = -ek_0 \frac{1}{1 + \exp(-\Delta G_H/k_B T)}. \quad (4)$$

If $\Delta G_H > 0$, the proton transfer is endothermic, and it should be

$$i_0 = -ek_0 \frac{1}{1 + \exp(-\Delta G_H/k_B T)} \exp(-\Delta G_H/k_B T), \quad (5)$$

where k_0 is the rate constant set to 1 [58], which includes all effects related to the reorganization of the solvent during the proton transfer to the catalytic surface, and k_B is the Boltzmann constant.

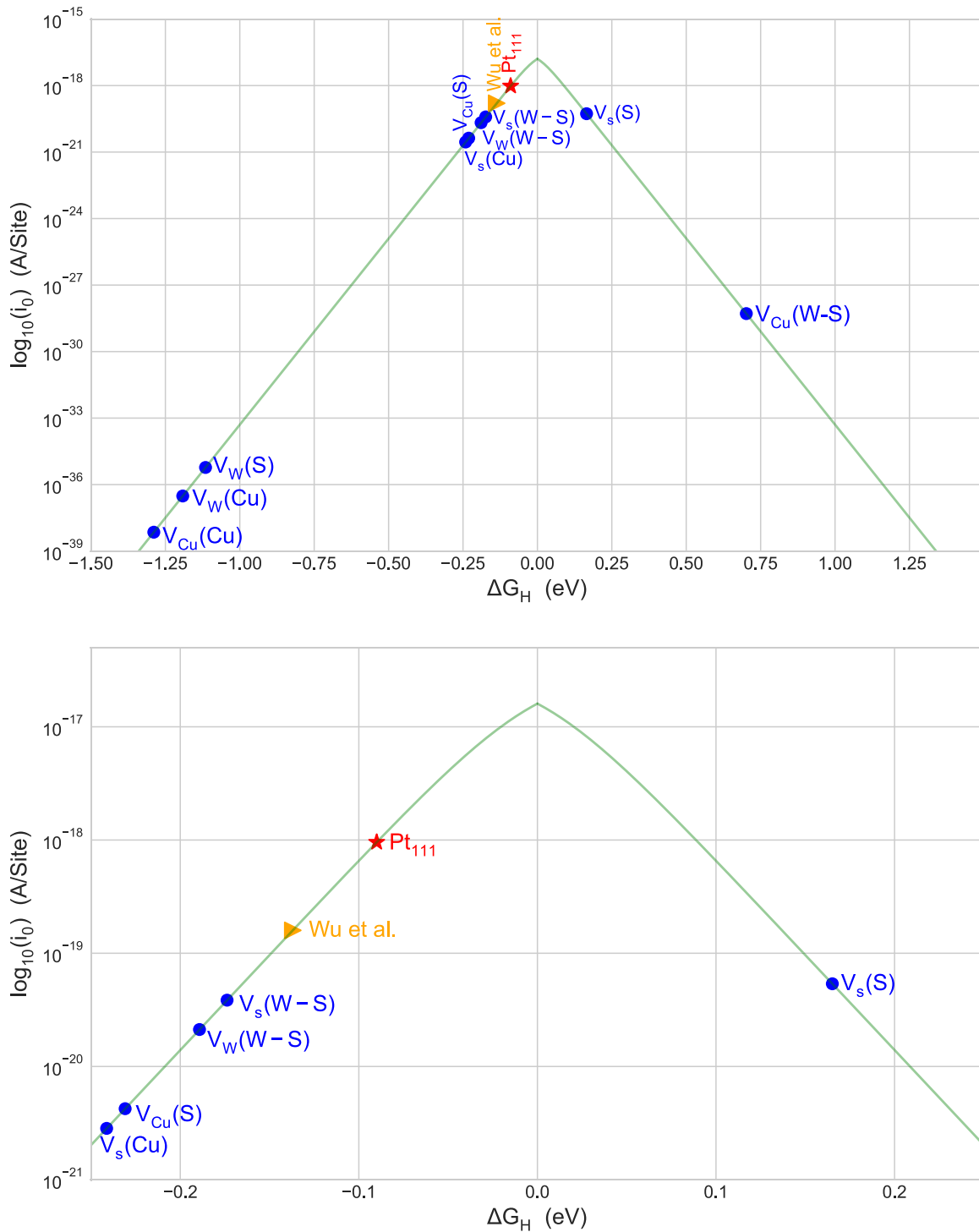


FIG. 10. Top: Volcano plot of exchange current density i_0 as a function of ΔG_H for the $V(Cu)@H^+$, $V(S)@H^+$, and $V(W)@H^+$ defective structures. Bottom: Close-up of the more favorable sites. The volcano curves of $Pt(111)$ and $V(s)$ from Ref. [14] are also shown.

The peak of the volcano should correspond to the maximum HER activity and then to the optimal HBE of an ideal catalyst. Figure 10 gathers the case of $Pt(111)$, the “gold standard” HER catalyst (with $\Delta G_H = -0.09$ eV), together with the results reported by Wu *et al.* [14]. The plot was calculated for two scenarios: an exothermic proton transfer ($\Delta G_H < 0$) and an endothermic proton transfer ($\Delta G_H > 0$). We found that $V_S(S-W)$ and $V_{Cu}(S-W)$ have ΔG_H closer to

the top of the volcano, providing the more favorable exchange current densities and lower overpotential [59] to be used for electrocatalysts. The other sites are too weak to be active in HER because they require high energy for desorption of the adsorbed H^* . The catalytic activity of the $V_S(S)$ and $V_{Cu}(W-S)$ sites on the left side of the volcanos is limited by the desorption of the products. In contrast to conventional metallic catalysts where electrons or holes are delocalized

on numerous atomic sites, the vacancy states in the sulfur defect point structure are formed by weak hybridization of d states (see Fig. 9); the active site of the V(S) introduced is an atom-sized defect embedded in the basal surface with the ability to trap charges. As a consequence, the binding of protons and electron transfers can proceed independently at the active site during HER, which in turn facilitates the capture of electrons at the bridge of the W-S active site [60].

IV. CONCLUSIONS

We used first-principles quantum mechanics calculations to study the structural stability and the role of native defects, specifically vacancies, in the HER reactivity of a Cu_2WS_4 monolayer. The stability of the pristine structure was determined by means of phonon and elastic constant calculations. We also found that 2D Cu_2WS_4 has a ductile behavior, which makes it mechanically favorable for catalytic applications. In addition, the most favored defect structure was found using Freysoldt's methodology. The calculation of both formation energy and enthalpy indicates the feasibility of Cu defects, which are more favorable than W and S defects. However, the analysis of catalytic properties showed that the choice of the nature of the defect does not make a big difference. The use of anionic or cationic defects on the basal surface of the Cu_2WS_4 monolayer gives a comparable HER power factor. An analysis of the electronic patterns of different defective structures showed that both V(S) and V(Cu) retained their semiconducting nature, in contrast to V(W), which fa-

vors metallization. Among defective structures, V(S) gives the largest HER activity because one electron from the adsorbed hydrogen fills spin-up channels in the band structure, forming a strong hybridization and then a strong bond. The adsorption on this structure modifies the energetic structure more strongly than on the two other studied vacancies. This behavior is correlated with conclusions drawn from the volcano-like plot of the HER reaction. Note that the present investigation focused on the analysis of the Cu_2WS_4 system. This analysis is of fundamental interest, but additional analyses are required to evaluate structural aspects such as the thickness of the material and the substrate where it is grown, which could affect the electrocatalytic properties.

ACKNOWLEDGMENTS

T.O. is thankful for the financial support obtained through PRFU B00L02EP130220230001. D.E. thanks the Spanish Ministry of Science and Innovation (MCIN/AEI/10.13039/501100011033) for support under Grants No. PID2019-106383GB-C41 and No. RED2018-102612-T and Generalitat Valenciana (GV) under Prometeo Grant No. CIPROM/2021/075-GREENMAT and Grant No. MFA/2022/007. This study is part of the Advanced Materials program supported by MCIN and GV with funding from European Union NextGenerationEU (PRTR-C17.I1). We thank GENCI and Pôle Messin de Modélisation et Simulation for providing computational resources, Allocation No. 2020-A0080910433.

- [1] D. Er, H. Ye, N. C. Frey, H. Kumar, J. Lou, and V. B. Shenoy, Prediction of enhanced catalytic activity for hydrogen evolution reaction in Janus transition metal dichalcogenides, *Nano Lett.* **18**, 3943 (2018).
- [2] H. Wu, X. Li, R. Zhang, and J. Yang, Proposal of a stable B_3S nanosheet as an efficient hydrogen evolution, *J. Mater. Chem. A* **7**, 3752 (2019).
- [3] S. Sun, G. Wang, Y. Zhou, F. Wang, and X. Xia, High-performance $\text{Ru}@\text{C}_4\text{N}$ electrocatalyst for hydrogen evolution reaction in both acidic and alkaline solutions, *ACS Appl. Mater. Interfaces* **11**, 19176 (2019).
- [4] Y. Zheng, Y. Jiao, M. Jaroniec, and S. Z. Qiao, Advancing the electrochemistry of the hydrogen-evolution reaction through combining experiment and theory, *Angew. Chem., Int. Ed.* **54**, 52 (2015).
- [5] L. Shi, C. Ling, Y. Ouyang, and J. Wang, High intrinsic catalytic activity of two-dimensional boron monolayers for the hydrogen evolution reaction, *Nanoscale* **9**, 533 (2017).
- [6] L. Luo, B. Wang, J. Jiang, M. Fitzgerald, Q. Huang, Z. Yu, H. Li, J. Zhang, J. Wei, C. Yang, H. Zhang, L. Dong, and S. Chen, Heavy metal contaminations in herbal medicines: Determination, comprehensive risk assessments and solutions, *Front. Pharmacol.* **11**, 595335 (2020).
- [7] H. Li, C. Tsai, A. L. Koh, L. Cai, A. W. Contryman, A. H. Fragapane, J. Zhao, H. S. Han, H. C. Manoharan, F. A. Pedersen, J. K. Nørskov, and X. Zheng, Activating and optimizing MoS_2 basal planes for hydrogen evolution through the formation of strained sulphur vacancies, *Nat. Mater.* **15**, 48 (2016).
- [8] Y. R. An, X. L. Fan, Z. F. Luo, and W. M. Lau, Nanopolygons of monolayer MS_2 : Best morphology and size for HER catalysis, *Nano Lett.* **17**, 368 (2017).
- [9] B. Guo, K. Yu, H. Li, R. Qi, Y. Zhang, H. Song, Z. Tang, Z. Zhu, and M. Chen, Coral-shaped MoS_2 decorated with graphene quantum dots performing as a highly active electrocatalyst for hydrogen evolution reaction, *ACS Appl. Mater. Inter.* **9**, 3653 (2017).
- [10] R. Luo, M. Luo, Z. Wang, P. Liu, S. Song, X. Wang, and M. Chen, The atomic origin of nickel-doping-induced catalytic enhancement in MoS_2 for electrochemical hydrogen production, *Nanoscale* **11**, 7123 (2019).
- [11] X. C. Yan, Y. Jia, and X. D. Yao, Defects on carbons for electrocatalytic oxygen reduction, *Chem. Soc. Rev.* **47**, 7628 (2018).
- [12] Y. Jia, K. Jiang, H. Wang, and X. Yao, The role of defect sites in nanomaterials for electrocatalytic energy conversion, *Chem* **5**, 1371 (2019).
- [13] Q. Wu, Y. Ma, R. Peng, B. Huang, and Y. Dai, Single-layer Cu_2WS_4 with promising electrocatalytic activity towards hydrogen evolution reaction, *ACS Appl. Mater. Interfaces* **11**, 45818 (2019).
- [14] Q. Wu, W. Wei, X. Lu, B. Huang, and Y. Dai, Computational screening of defective group IVA monochalcogenides as efficient catalysts for hydrogen evolution reaction, *J. Phys. Chem. C* **123**, 11791 (2019).
- [15] D. Deng, L. Yu, X. Pan, S. Wang, X. Chen, P. Hu, L. Sun, and X. Bao, Size effect of graphene on electrocatalytic activation of oxygen, *Chem. Commun.* **47**, 10016 (2011).

- [16] S. Dou, L. Tao, R. L. Wang, S. El Hankari, R. Chen, and S. Y. Wang, Plasma-assisted synthesis and surface modification of electrode materials for renewable energy, *Adv. Mater.* **30**, 1705850 (2018).
- [17] X. Wang, L. Z. Zhuang, Y. Jia, H. L. Liu, X. C. Yan, L. Z. Zhang, D. J. Yang, Z. H. Zhu, and X. D. Yao, Plasma-triggered synergy of exfoliation, phase transformation and surface engineering in cobalt diselenide for enhanced water oxidation, *Angew. Chem., Int. Ed.* **57**, 16421 (2018).
- [18] M. Niaounakis, Surface treatment, in *Biopolymers: Processing and Products* (Elsevier, Amsterdam, 2014), p. 303.
- [19] Y. Yan, L.-C. Xu, E. A. Vogler, and C. A. Siedlecki, Contact activation by the intrinsic pathway of blood plasma coagulation hemocompatibility of biomaterials for clinical applications, in *Blood-Biomaterials Interactions* (Elsevier, Amsterdam, 2018), pp. 3–28.
- [20] E. A. Pruss, B. S. Snyder, and A. M. Stacy, A new layered ternary sulfide: Formation of Cu_2WS_4 by reaction of WS_4^{2-} and Cu^+ ions, *Angew. Chem., Int. Ed.* **32**, 256 (1993).
- [21] C. J. Crossland, P. J. Hickey, and J. S. O. Evans, The synthesis and characterization of Cu_2MX_4 ($\text{M} = \text{W}$ or Mo ; $\text{X} = \text{S}$, Se or S/Se) materials prepared by a solvothermal method, *J. Mater. Chem.* **15**, 3452 (2005).
- [22] B. Polyakov, A. Kuzmin, S. Vlassov, E. Butanovs, J. Zideluns, J. Butikova, R. Kalendarev, and M. Zubkins, A comparative study of heterostructured CuO/CuWO_4 nanowires and thin films, *J. Cryst. Growth* **480**, 78 (2017).
- [23] J. Y. Zheng, G. Song, C. W. Kim, and Y. S. Kang, Facile preparation of p-CuO and p-CuO/n-CuWO₄ junction thin films and their photoelectrochemical properties, *Electrochim. Acta* **69**, 340 (2012).
- [24] N. F. Andrade Neto, Y. G. Oliveira, J. H. O. Nascimento, M. R. D. Bomio, and F. V. Motta, Influence of pH variation on CuWO_4 , $\text{CuWO}_4/\text{WO}_3$ and CuWO_4/CuO structures stabilization: Study of the photocatalytic properties under sunlight, *J. Mater. Sci. Mater. Electron.* **31**, 18221 (2020).
- [25] A. P. Tiwari, A. Azam, T. G. Novak, O. Prakash, and S. Jeon, Chemical strain formation through anion substitution in Cu_2WS_4 for efficient electrocatalysis to water dissociation, *J. Mater. Chem. A* **6**, 7786 (2018).
- [26] C. Freysoldt, B. Grabowski, T. Hickel, J. Neugebauer, G. Kresse, A. Janotti, and C. G. Van de Walle, First-principles calculations for point defects in solids, *Rev. Mod. Phys.* **86**, 253 (2014).
- [27] D. Broberg, B. Medasani, N. E. R. Zimmermann, G. Yu, A. Canning, M. Haranczyk, M. Asta, and G. Hautier, PyCDT: A Python toolkit for modeling point defects in semiconductors and insulators, *Comput. Phys. Commun.* **226**, 165 (2018).
- [28] X. Hu, W. Shao, X. Hang, X. Zhang, W. Zhu, and Y. Xie, Superior electrical conductivity in hydrogenated layered ternary chalcogenide nanosheets for flexible all-solid-state supercapacitors, *Angew. Chem., Int. Ed.* **55**, 5733 (2016).
- [29] G. Kresse and J. Furthmüller, Efficiency of ab-initio total energy calculations for metals and semiconductors using a plane-wave basis set, *Comput. Mater. Sci.* **6**, 15 (1996).
- [30] G. Kresse and J. Hafner, *Ab initio* molecular dynamics for liquid metals, *Phys. Rev. B* **47**, 558 (1993).
- [31] H. Z. Guedda, T. Ouahrani, A. Morales-García, R. Franco, M. A. Salvadó, P. Pertierra, and J. M. Recio, Computer simulations of 3C-SiC under hydrostatic and non-hydrostatic stresses, *Phys. Chem. Chem. Phys.* **18**, 8132 (2016).
- [32] P. E. Blöchl, Projector augmented-wave method, *Phys. Rev. B* **50**, 17953 (1994).
- [33] J. P. Perdew, K. Burke, and M. Ernzerhof, Generalized Gradient Approximation Made Simple, *Phys. Rev. Lett.* **77**, 3865 (1996).
- [34] H. J. Monkhorst and J. D. Pack, Special points for Brillouin-zone integrations, *Phys. Rev. B* **13**, 5188 (1976).
- [35] S. Grimme, J. Antony, S. Ehrlich, and H. Krieg, A consistent and accurate ab initio parametrization of density functional dispersion correction (*DFT - D*) for the 94 elements $H - \text{Pu}$, *J. Chem. Phys.* **132**, 154104 (2010).
- [36] S. Grimme, S. Ehrlich, and L. Goerigk, Effect of the damping function in dispersion corrected density functional theory, *J. Comput. Chem.* **32**, 1456 (2011).
- [37] G. J. Martyna, M. L. Klein, and M. Tuckerman, Nose-Hoover chains: The canonical ensemble via continuous dynamics, *J. Chem. Phys.* **97**, 2635 (1992).
- [38] S. Nosé, A molecular dynamics method for simulations in the canonical ensemble, *Mol. Phys.* **52**, 255 (1984).
- [39] S. Nosé, A unified formulation of the constant temperature molecular dynamics methods, *J. Chem. Phys.* **81**, 511 (1984).
- [40] A. Togo and I. Tanaka, First-principles phonon calculations in materials science, *Scr. Mater.* **108**, 1 (2015).
- [41] X. Gonze and C. Lee, Dynamical matrices, born effective charges, dielectric permittivity tensors, and interatomic force constants from density-functional perturbation theory, *Phys. Rev. B* **55**, 10355 (1997).
- [42] J. K. Nørskov, J. Rossmeisl, A. Logadottir, L. Lindqvist, J. R. Kitchin, T. Bligaard, and H. Jonsson, Origin of the overpotential for oxygen reduction at a fuel-cell cathode, *J. Phys. Chem. B* **108**, 17886 (2004).
- [43] J. Greeley, T. F. Jaramillo, J. Bonde, I. Chorkendorff, and J. K. Nørskov, Computational high-throughput screening of electrocatalytic materials for hydrogen evolution, *Nat. Mater.* **5**, 909 (2006).
- [44] M. Huang, S.-S. Wang, Y.-N. Wu, and S. Chen, Defect Physics of Ternary Semiconductor ZnGeP_2 With a High Density of Anion-Cation Antisites: A First-Principles Study, *Phys. Rev. Appl.* **15**, 024035 (2021).
- [45] J. Heyd, G. E. Scuseria, and M. Ernzerhof, Hybrid functionals based on a screened Coulomb potential, *J. Chem. Phys.* **118**, 8207 (2003).
- [46] L. Wang, K. Zhang, J. Luo, J.-Y. Ma, W. Ji, Q. Hong, H. Xu, W. Huang, N. Yan, and Z. Qu, Metastable facet-controlled Cu_2WS_4 single crystals with enhanced adsorption activity for gaseous elemental mercury, *Environ. Sci. Technol.* **55**, 5347 (2021).
- [47] L. Qin, Z. Wen, X. Zhang, K. Zhang, Y. Lin, L. Song, X. J. Wu, and X. Qiu, Multiphonon raman scattering and strong electron-phonon coupling in 2D ternary Cu_2MoS_4 nanoflakes, *J. Phys. Chem. Lett.* **11**, 8483 (2020).
- [48] V. Wang, N. Xu, J. C. Liu, G. Tang, and W. T. Geng, VASPKIT: A user-friendly interface facilitating high-throughput computing and analysis using VASP code, *Comput. Phys. Commun.* **267**, 108033 (2021).
- [49] See Supplemental Material at <http://link.aps.org/supplemental/10.1103/PhysRevMaterials.7.025403> for additional information on calculated elastic constants, convergence tests, constraints used for determining stability conditions, calculated

- ΔG_H for the active sites, chemical potential phase diagrams, and calculated electronic densities and band structure.
- [50] M. Born and H. Huang, *Dynamical Theory of Crystal Lattices* (Clarendon, Oxford, 1954).
- [51] F. Mouhat and F. X. Coudert, Necessary and sufficient elastic stability conditions in various crystal systems, *Phys. Rev. B* **90**, 224104 (2014).
- [52] Y. Yin, Y. Wu, G. Chen, and W.-J. Yin, Double perovskite $\text{Ba}_2\text{BiTaO}_6$ as a promising p-type transparent conductive oxide: A first-principles defect study, *J. Appl. Phys.* **127**, 175703 (2020).
- [53] J. Dabrowski and G. Kissinger, Supercell-size convergence of formation energies and gap levels of vacancy complexes in crystalline silicon in density functional theory calculations, *Phys. Rev. B* **92**, 144104 (2015).
- [54] C. Freysoldt and J. Neugebauer, First-principles calculations for charged defects at surfaces, interfaces, and two-dimensional materials in the presence of electric fields, *Phys. Rev. B* **97**, 205425 (2018).
- [55] J. Buckeridge, D. O. Scanlon, A. Walsh, and C. R. A. Catlow, Automated procedure to determine the thermodynamic stability of a material and the range of chemical potentials necessary for its formation relative to competing phases and compounds, *Comput. Phys. Commun.* **185**, 330 (2014).
- [56] Y. Huang, C. Wang, X. Chen, D. Zhou, J. Du, S. Wang, and L. Ning, First-principles study on intrinsic defects of SnSe, *RSC Adv.* **7**, 27612 (2017).
- [57] T. Ouahrani, A. B. Garg, R. Rao, P. Rodríguez-Hernández, A. Muñoz, M. Badawi, and D. Errandonea, High-Pressure properties of wolframite-type ScNbO_4 , *J. Phys. Chem. C* **126**, 4664 (2022).
- [58] J. K. Nørskov, T. Bligaard, A. Logadottir, J. R. Kitchin, J. G. Chen, S. Pandelov, and U. Stimming, Trends in the exchange current for hydrogen evolution, *J. Electrochem. Soc.* **152**, J23 (2005).
- [59] T. Ouahrani, A. Daouli, M. Badawi, L. Bendaoudi, A. Morales-Garcia, and D. Errandonea, Understanding the thermodynamic, dynamic, bonding, and electrocatalytic properties of low dimensional MgPSe_3 , *Dalton Trans.* **51**, 9689 (2022).
- [60] K. Y. Kim, J. Lee, S. Kang, Y.-W. Son, H. W. Jang, Y. Kang, and S. Han, Role of hyper-reduced states in hydrogen evolution reaction at sulfur vacancy in MoS_2 , *ACS Catal.* **8**, 4508 (2018).